Nanoscale

Accepted Manuscript

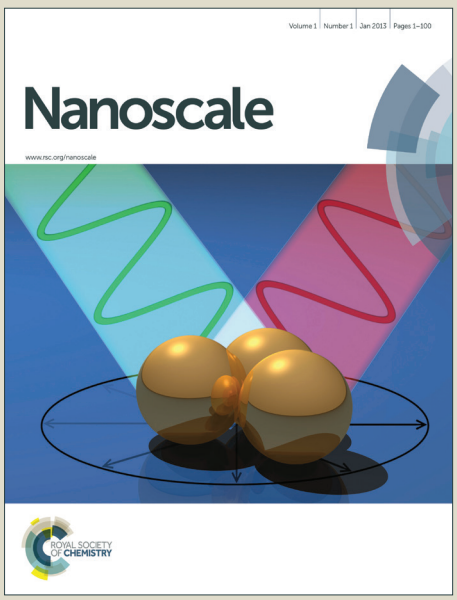

ROYAL SOCIETY OF CHEMISTRY

www.rsc.org/nanoscale

Shear Response of Copper Bicrystal with ∑11 Symmetric and Asymmetric Tilt Grain Boundaries by Molecular Dynamics Simulation

Liang Zhang*, Cheng Lu*, Kiet Tieu, Xing Zhao, Linqing Pei

School of Mechanical, Materials and Mechatronic Engineering, University of Wollongong, Wollongong, NSW 2522, Australia.

*Corresponding author. Tel.:+6142214639; fax:+61242213101; E-mail: chenglu@uow.edu.au (C. Lu); lz592@uowmail.edu.au (L. Zhang)

Grain boundaries (GBs) are important microstructure features and can significantly affect the properties of nanocrystalline materials. Molecular Dynamics simulation was carried out in this study to investigate the shear response and deformation mechanisms of symmetric and asymmetric Σ11<1 1 0> tilt GBs in copper bicrystal. Different deformation mechanisms were reported, depending on GB inclination angles and equilibrium GB structures, including GB migration coupled to shear deformation, GB sliding caused by local atomic shuffling, and dislocation nucleation from GB. The simulation showed that migrating Σ11(1 1 3) GB under shear can be regarded as sliding of GB dislocations and their combination along the boundary plane. A non-planar structure with dissociated intrinsic stacking fault was prevalent in Σ11 asymmetric GBs of Cu. This type of structure can significantly increase the ductility of bicrystal models under shear deformation. Grain boundary can be a source of dislocation and migrate itself at different stress levels. The intrinsic free volume involved in the grain boundary area was correlated to dislocation nucleation and GB sliding, while the dislocation nucleation mechanism can be different for a grain boundary due to its different equilibrium structures.

†Electronic Supplementary Information (ESI) available: [Movies show the evolution of different grain boundaries under shear deformation: S-0, S-54.74, S-70.53-A, S-70.53-B, S-90]

1. Introduction

Many recent experimental and simulation works indicated that the dislocation activities in the interior grains lessen when the average grain size is less than 100 nm, whereas mechanisms mediated by the grain boundary (GB) become dominant[1, 2]. A strong interplay between intergranular and intragranular deformation processes was found in nanocrystalline metals, so understanding how the nanoscale grain boundary networks affect deformation is critical. The grain boundary in nanocrystalline structures can restrict dislocation propagation and also act as a source for new dislocations which affect the detailed dynamics of dislocation-mediated plasticity[3]. Particularly, grain boundary accommodation mechanisms such as GB sliding, GB migration, and grain rotation has long been recognized as important mechanisms of deformation for very small grain sizes[4]. Unlike experimental observation, which is difficult to perform at nanoscale and is very time consuming, atomistic simulation has a lot of advantages. For example, molecular dynamics (MD) simulation helps in the study of plasticity because the deformation conditions can be controlled and a detailed investigation of the underlying atomic scale processes can be made, and it results in extremely detailed atomistic information. Moreover, the visualisation tools[5, 6] and the sophisticated automated dislocation detection techniques[7-9] have improved greatly in recent years, so we can now gather more information at the atomic scale.

While the polycrystalline model with grain boundary networks constructed by the Voronoi tessellation[10] produced microstructures with topological properties closer to the experimental ones, simple bicrystal atomic configuration geometry is often used to systematically study the correlation of grain boundary structures and material properties, which makes it ideal for studying high-angle coincident site lattices (CSL). Bicrystal models have been used in many previous research works with fruitful results; for instance Sansos and Molinari[11, 12] correlated individual failure mechanisms to the presence of certain structural units along the interface plane using the quasi-continuum method, and reported different failure mechanisms of bicrystal Cu and Al, depending on their grain boundary structures when subjected to tensile and shear deformation, including GB sliding by atoms shuffling, nucleation of partial dislocations from GB, and GB migration. Using MD simulations, Cahn and Mishin *et al*[13], and Wan *et al*[14] showed that some symmetric tilt GBs can migrate when a shear deformation is applied parallel to the GB plane, and they also provided a correlation between the shear stress, the structure of grain boundaries (in terms of structural units) and their normal motion. Koning *et al*[15, 16] and Jin *et al*[17, 18] used bicrystal models to investigate the barrier effect of different GBs and twin boundaries with respect to dislocations, and then proposed the conditions under which dislocation transmission can occur across a grain boundary. Spearot and McDowell *et al*[19-21] used MD simulations to examine the dislocation nucleation from different GB planes in bicrystal Cu and Al, by focusing on the evolution of the grain boundary structures during dislocation nucleation and the resulting structure of the grain boundary after dislocation emission. Because bicrystal systems enable a more controlled investigation of specific GB properties, we will take full advantage of the bicrystal model in this study to investigate the mechanical properties and deformation mechanisms of certain grain boundaries.

Most of the experiments and simulations conducted so far focused primarily on symmetric tilt GBs, whereas the less studied cases of asymmetric tilt GBs are more complex but pose new and interesting questions. For example, Bachurin *et al*[22] carried out an atomistic simulation to study the interaction of dislocations with some GBs in Ni bicrystal, and showed that symmetric GBs and asymmetric GBs can play a different role in blocking the incoming dislocations. Tschopp *et al*[23] and Zhang *et al*[24] used an MD simulation to investigate dislocation nucleation from both symmetric and asymmetric Σ3<1 1 0> tilt GBs and Σ5<0 0 1> tilt GBs under uniaxial tension, and found that the mechanical properties of GB depend upon GB misorientation and the inclination of the GB plane. The simulation results from Trautt and Mishin *et al*[25], Hao *et al*[26], and Fensin *et al* [27] indicated that stress-driven GB migration not only occurs in symmetric GBs but also in some asymmetric GBs. Although this previous work on asymmetric GBs has increased our understanding of the structures and energy on these boundaries, and provided an insight into related GB properties, our understanding of deformation mechanisms of asymmetric GBs at the atomic scale is still limited. In this study, we carried out molecular dynamics simulations to investigate the shear response of Cu bicrystal with symmetric and asymmetric Σ11<1 1 0> tilt GBs, and reported different mechanical properties and deformation mechanisms exist, depending on the GB inclination angles and local GB structures.

2. Simulation methodology

In this study MD simulations were carried out using the parallel molecular dynamics code LAMMPS[28] with the embedded-atom method (EAM) potentials for Cu developed by Mishin *et al*[29]. A bicrystal model is created by constructing two separate crystal lattices (grain-A and grain-B in Fig.1) with different crystallographic orientation and joining them together along the Y axis. A periodic boundary condition was applied in the X and Z directions while a non-periodic boundary condition was applied in the Y direction. Details of the grain boundary and the dimensions of the bicrystal models are presented in Table-1.

Table.1 Grain boundary details and dimensions of bicrystal models.

Boundary type	Inclination angle Φ (°)	Boundary plane (h k l)A/B	Boundary energy γ (mJ/m^2)	Structural unit period	Model dimensions X×Y×Z (Å)
Symmetric	0	(1 1 -3)/(1 1 3)	307	|…C.C.C.C.C…|	144.4×216.6×36.1
Asymmetric	54.74	(2 2 5)/(4 4 1)	662	|…DCE.DCE…|	146.9×218.4×36.1
Asymmetric	70.53-A	(5 5 7)/(7 7 -1)	706	|…DDE.DDE…|	152.7×216.6×36.1
Asymmetric	70.53-B	(5 5 7)/(7 7 -1)	702	|…DED.DED…|	152.7×216.6×36.1
Symmetric	90	(3 3 2)/(3 3 -2)	722	|…ED.ED.ED…|	144.4×216.6×36.1

The equilibrium GB structure was prepared using a combination of molecular statics and MD simulations. A molecular statics calculation using an energy minimization procedure with a standard conjugate-gradient algorithm was carried out to determine the minimum energy configuration of each grain boundary. A number of initial "starting positions" of grain-A and grain-B were tested to find the most favored GB structures from the point of view of energy[30-33]. Notice that, while changing the positions of the two grains before energy minimization procedure, an overlap between the grains may result in an unphysically short distance between two atoms. If the pairs of atoms whose distance of separation is within the cutoff distance, then one atom was arbitrarily deleted in grain-B. In the simulation, the cutoff distance was specified as $0.5a_0$ to delete the atoms which have unphysically short distance to others and insure the first nearest neighbor atoms ($\sqrt{2}/2a_0$) are not found within the cutoff distance for the crystal structure, where a_0 is the lattice constant. After the procedure of energy minimization, the energy of each GB structure is then calculated and compared to find the possible global minimum energy configuration. After the minimum energy structure was attained, the simulation model was equilibrated using MD in the isobaric-isothermal (NPT) ensemble at a pressure of 0 bar and a temperature of 10 K for 20 ps. Our primary goal in this study is to investigate the shear response of different GBs and its connection with the structure evolution, so the simulation temperature was set at 10 K throughout the simulations to avoid thermal disturbance of atoms at high temperature.

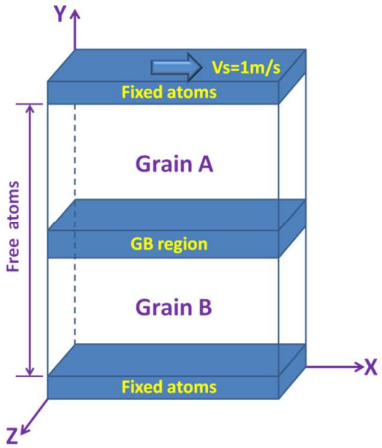

Figure-1. Schematic of shear deformation applied onto the bicrystal model. Atoms on the top of grain-A and atoms at the bottom of grain-B are fixed, all the other atoms in the model were set free. A constant shear velocity V_s=1m/s parallel to the boundary plane was applied on the fixed area of grain A along the X direction.

Once the equilibrium state of GB was reached, a shear deformation was applied to bicrystal model to investigate the mechanical response of the GBs. Atoms on the top of grain-A and atoms at the bottom of grain-B were fixed, the thickness of each fixed slab was approximately twice the cutoff radius of atomic interactions[13], while all the other atoms in the model were set free. Fig.1 shows the schematic of the computational cell in our simulations. A constant shear velocity $V_s = 1\mathrm{m/s}$ (about $4.6 \times 10^7/\mathrm{s}$ shear strain in this study) parallel to the boundary plane was applied onto the fixed area of grain-A in the X direction. The fixed atoms in grain-A do not participate in MD simulations and only move with 1m/s as a rigid body, while the fixed atoms in grain-B remained stationary. Stress and temperature calculations were performed on the dynamic atoms between the two fixed slabs, while the stress tensor was calculated by the standard virial expression. Throughout the MD simulation, the NPT method was adopted and the time increment of simulations was fixed at 1 fs.

The visualization tools Atomeye[5] and Ovito[6] were used to illustrate the bicrystal models. The common neighbor analysis (CNA) technique[34] was used to identify defects in the structure and its evolution during the simulations. It gives a classification of all the atoms by their local crystallinity. For metals of fcc structure type, three categories of atoms in the system were identified: atoms of fcc structure order, atoms of hcp structure order and atoms of other structure order. Within this scheme, a single layer of hcp atoms represents a twin boundary, two adjacent hcp atom layers manifest an intrinsic stacking fault, and two hcp atom layers with an intermediate fcc atom layer represent an extrinsic stacking fault. The Crystal Analysis Tool developed by Stukowski[8, 9] was used to detect dislocations in this study. The robust code supports a wide range of crystal lattice types and can identify partial dislocations as well as grain boundary dislocations. Also, it can convert the identified dislocations into continuous lines and computerize their Burgers vectors.

3. Results and discussion

3.1 Grain boundary structure

Two symmetric (Φ=0°, Φ=90°) and two asymmetric (Φ=54.74°, Φ=70.53°) Σ11<1 1 0> (θ=50.5°) tilt grain boundaries were

investigated in this study, where θ is the misorientation angle of the two grains constructed in the bicrystal model, and Φ is the inclination angle of the GB plane which is defined as the angle between the boundary plane and the bisector of the misorientation angle θ. The structures of the selected two asymmetric GBs can represent the typical structure of Σ11<1 1 0> asymmetric GBs in the wide range of inclination angle (0°<Φ<90°)[35, 36]. Fig.2 shows the equilibrium GB structures that resulted from the energy minimization procedure and subsequent MD relaxation at 10 K with zero stress state for Cu bicrystal. The GB structure area is identified using the common neighbor analysis (CNA) technique[34]. Note that for the asymmetric Σ11(5 5 7)/(7 7 $\bar{1}$) Φ=70.53° GB, two different equilibrium structures with a similar GB energy (706 mJ/m^2 and 702 mJ/m^2) was found after constructing the model. Since the GB energy of the two structures are very close and are much lower than the value of other structures, both of them will be considered in this study. For convenience, the two different GB structures will be known as Φ=70.53°-A and Φ=70.53°-B (see in Fig.2). Structural units as defined by Rittner and Seidman[37] were used to illustrate the boundary structures, while the symmetric Σ11(1 1 3) Φ=0° GB and Σ11(3 3 2) Φ=90° GB was composed entirely of C and E structural units respectively. For the asymmetric Σ11(2 2 5) Φ=54.74° GB, the boundary area is a combination of C and E units at the boundary plane and a D unit at the termination of an intrinsic stacking fault that extended from the boundary plane. Similarly, a dissociated GB structure was also observed in the two structures of Σ11(5 5 7) Φ=70.53° GB, where the periodic units can be described as "DDE" and "DED" respectively.

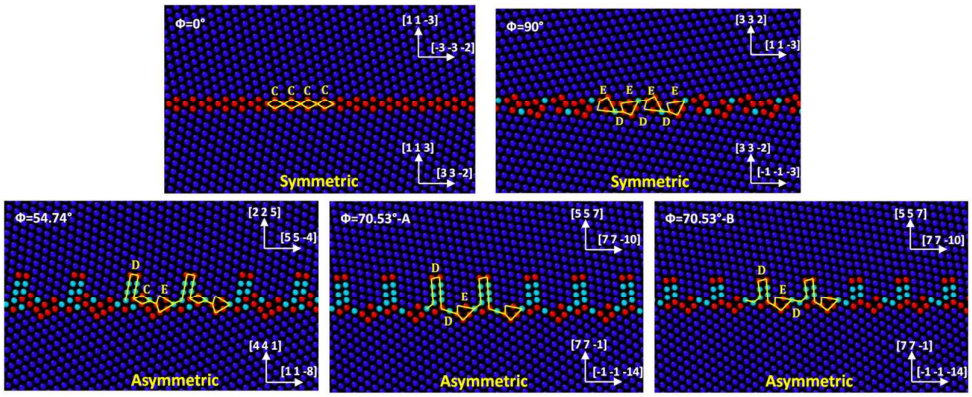

Figure-2. The equilibrium structures of the Σ11 symmetric and asymmetric GBs obtained by the energy minimization procedure and subsequent MD relaxation at 10 K. The images are viewed along the [1 $\bar{1}$ 0] tilt axis and are colored according to the CNA parameter. Atoms with perfect fcc structures are blue, the red atoms organize the GB plane and the dislocation core, and the continuous light blue atoms represent the stacking fault. The boundary normal vector of the two grains are marked on the right hand side for each GB. The structural units at each boundary plane are outlined by the solid line and marked by C, D, and E.

3.2 The shear response of Σ11(1 1 3) Φ=0° GB

The shear stress of the bicrystal model with Σ11(1 1 3) GB as a function of simulation time is plotted in Fig.3(a). After reaching its critical shear stress (3.61 GPa) the Σ11(1 1 3) GB showed a sliding-migration coupling motion with a further increase of shear deformation where the upper grain slide was relative to the lower grain while GB migrated from the centre of the bicrystal to the upper grain. The four abrupt drops in the stress curve correspond to the four intensive GB migrations (see movie 'S-0', where the atoms with perfect fcc structures were removed to facilitate the view of defective structures). The movement of high-angle GBs in the coupled manner under stress can be regarded as the motion of perfect GB dislocation[38] where in this case the GB plane remained almost flat during the coupling motion, which suggested that the sliding of Σ11(1 1 3) GB resulted from the motion of GB dislocations with Burgers vector parallel to the GB plane. Of the different GB dislocations formed by the crystal lattice dislocations, perfect GB dislocations with Burgers vector **b**=(1/22)<3 3 2> satisfy this condition. This theoretical speculation was identified by Fukutomi and Kamijio in their experimental observation on bicrystal aluminum[39] as well as in our MD simulation.

The detailed process of GB coupling motion explained in Fig.3. Fig.3(b) and (c) are two consecutive snapshots from the MD results that indicate the first GB migration event. Fig.3(d) shows the dislocation extracted from the corresponding MD results by the Crystal Analysis Tool [8, 9]. All the C structural units were in the same plane until t=1.584 ns, when a step at the GB plane appeared, as shown in Fig.3(b). The left part of GB_1 has migrated upwards to GB_2 (marked by the dashed line) by a distance (H1) of two atomic layer heights along the [1 1 3] direction. The GB step, or GB disconnection was caused by the GB dislocation **b**=(1/22)[3 3 2], as marked with 'GB dislocation 1' in Fig.3(b). It is indicated by the extracted red line in Fig.3(d) at t=1.584 ns. This was consistent with the previous experiment result[39]. However, unlike the experimental observation, the simulation showed that (1/22)<3 3 2> was not the only type of GB dislocation existing in the process of GB migration. With a further increase of shear deformation, while the former step between GB_1 and GB_2 still existed, another two steps appeared at the boundary area which introduced two new GB planes indexed as GB_3 and GB_4 (see in Fig.3-c at t=1.586ns). Notice that the two steps are only one atom layer height (H2) along the [1 1 3] direction, indicating that another type of dislocation may exist in the boundary plane. This is confirmed in Fig.3(d) when the dislocations were detected at this time. It is easy to find that the red line with **b**=(1/22)[3 3 2] represents the former step, while the two blue lines with **b**=(1/22)[7 4 $\bar{1}$] indicate the two evolutive steps. The new type of GB dislocation is marked with 'GB dislocation 2' in Fig.3(c).

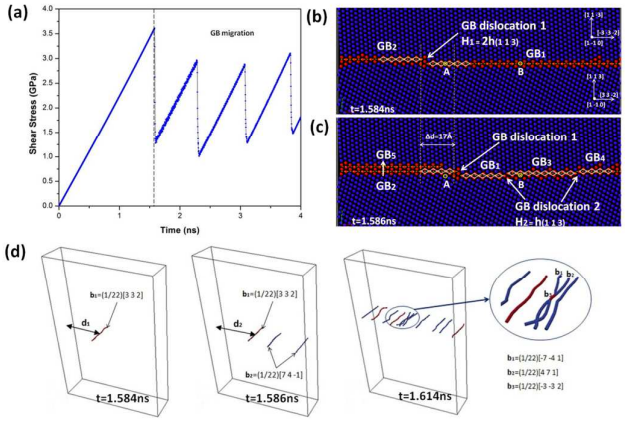

Figure-3. Shear response of Σ11(1 1 3) Φ=0° GB. (a) Shear stress as a function of simulation time. (b) and (c) Snapshots of the enlarged GB area at

t=1.584 ns and t=1.586 ns. Atoms with perfect fcc structures are blue, and the red atoms organize the GB plane. (d) Dislocation extracted from the corresponding MD results.

From Fig.3(b) to Fig.3(c), the step has moved along the grain boundary a distance (Δd=d2-d1) of about 17Å. Meanwhile, more of GB_1 has migrated to GB_2 which implies that the sliding of GB dislocation was closely connected to GB migration. Specifically, after GB dislocation had passed, atoms such as A and B, which were a coincidence site before the migration of GB_1 in Fig.3(b), are no longer a coincidence site in Fig.3(c). If all the GB atoms are uniquely arranged around the coincidence site, the GB is considered to migrate. Moreover, the migrating GB plane was not completed one layer after another, as shown in Fig.3(c), when the migration of GB_1 to GB_2 was still in progress due to the propogation of GB dislocation, the trailing part of GB_2 was already prepared for another migration to GB_5. The inconsonant movement of GB plane can result in a series of steps or disconnections at the boundary plane, indeed Fig.3(d) at t=1.614 ns shows that a number of GB dislocations (1/22)<3 3 2> (red lines) and (1/22)<7 4 1> (blue lines) coexist. As the experiment[39] and geometric analysis indicated, the coupling motion of Σ11(1 1 3) GB was attributed to a GB dislocation (1/22)<3 3 2> sliding along the GB plane. So how does GB dislocation (1/22)<7 4 1> work? Fig.3(c) shows that GB_4 was at the same height as GB_2, in other words, the two steps caused by the GB dislocation (1/22)<7 4 1> have the same effect on GB migration as the step result from the GB dislocation (1/22)<3 3 2>. It was naturally assumed there should be some correlation between the two types of GB dislocations where this assumption is identified in the enlarged area in Fig.3(d) at t=1.614 ns. The two blue lines with Burger's vectors $\mathbf{b_1}$ and $\mathbf{b_2}$ have merged into the red line with Burger's vector $\mathbf{b_3}$, which implies the (1/22)<7 4 1> dislocation can transform to (1/22)<3 3 2> dislocation through a GB dislocation reaction. This reaction can be described as,

$$(1/22)[\bar{7}\ \bar{4}\ 1] + (1/22)[4\ 7\ 1] \rightarrow (1/22)[\bar{3}\ \bar{3}\ 2]$$

In this study, the Burger vectors of boundary dislocations in all the equations of dislocation reaction was defined based on the upper lattice frame (grain-A).

3.3 The shear response of Σ11(2 2 5)/(4 4 1) Φ=54.74° GB

The shear stress of the bicrystal model with Σ11(2 2 5)/(4 4 1) GB as a function of simulation time is plotted in Fig.4(a) and shows that deformation of the bicrystal model occurred in four stages: elastic, plastic, strain-hardening and strain-softening. These stages are divided by the dashed line in Fig.4(a) and the corresponding deformation configurations are presented in Fig.4(b). In the elastic stage, the GB structure kept its initial equilibrium configuration until it reached the yield stress (σ_y=0.54 GPa). According to the Crystal Analysis results in Fig.4(c), the equilibrium boundary structure can be regarded as being composed of an array of GB dislocations with Burgers vector $\mathbf{b}=(1/6)[\bar{1}\ \bar{1}\ \bar{4}]$ and $\mathbf{b}=(1/3)[1\ 1\ \bar{1}]$. The onset of plasticity corresponded to the collective movement of the dissociated $1/6[1\ 1\ \bar{2}]$ Shockley partial dislocations from the GB plane and the extension of the intrinsic stacking fault behind (see in Fig.4-b at t=0.6 ns). It is interesting to see that the stress curve reached a plateau in the plastic stage, which indicated that the dislocations emitted from GB played a small role in accommodating the system stress, which was different from the previous finding where the stress curve started to drop once the dislocation became active[12, 19, 21, 24]. This was mainly due to the intrinsic structure of GB with the embryo dislocations where only a low stress can drive them to emit. Here, we describe it as dislocation "emission" instead of "nucleation" because the yield stress corresponded to the release of the dissociated partial dislocations rather than nucleating new dislocations from the GB plane into the bulk crystal lattice. During the emission process in stage-2, the boundary rearranged itself by adjusting positions of local atoms. This rearrangement can be regarded as a combination of GB dislocations that described by:

$$(1/6)[\bar{1}\ \bar{1}\ \bar{4}] + (1/3)[1\ 1\ \bar{1}] \rightarrow (1/6)[1\ 1\ \bar{6}]$$

Note that the propagation of dislocations was blocked when they reached the fixed area of the simulation model . After that, the stress curve reached the strain-hardening stage with a continuous stress increase without any new deformation mechanisms to release the system stress (see in Fig.4-b at t=1.2 ns). From a physical perspective, the fixed area in the model can be regarded as another grain boundary which helps to block the dislocation slipping. This always happens in polycrystalline materials where the grain boundaries hinder the transmission of dislocations and create a dislocation pile-up at the boundary and thereby make the materials hard to deform[40, 41]. The strain-hardening effect stops, i.e. the maximum shear stress (σ_y=2.51 GPa) has been reached, when the grain boundary begins to migrate, which leads to the strain-softening stage. The migration of GB downwards to the lower grain causes the upper grain to grow and the lower grain to shrink, while once again increasing the length of the intrinsic stacking fault. Fig.4-b (at t=2.12 ns) shows a snapshot of bicrystal configuration after two jumps of GB migration. The original GB position is indicated by the dashed line for comparison. It is worth noting that, based on the classic theory by Read and Shockley[42], the non-uniform structure of asymmetric GBs consist of more than two types of dislocations, which can block each other when gliding on the intersection planes and prevent a coupled motion. Therefore, the migration of asymmetric GBs was thought to be impossible, but recent observations of coupled GB motion in bicrystal experiments[43, 44] has suggested that this may not be true. The migration of Σ11(Φ=54.74°) asymmetric GB in our simulation study also confirmed this view. Crystal Analysis results indicated that the GB migrating process was accompanied by the GB dislocation decomposition with some embryonic Shockley partial dislocations. This process can be described as:

$$(1/6)[1\ 1\ \bar{6}] \rightarrow (1/3)[1\ 1\ \bar{2}] + (1/6)[\bar{1}\ \bar{1}\ \bar{2}]$$

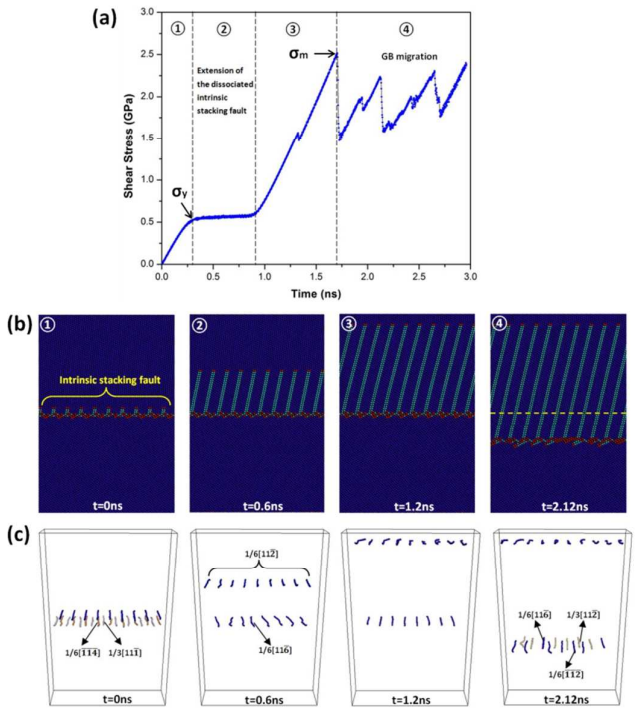

Figure-4. Shear response of ∑11(2 2 5)/(4 4 1) Φ=54.74° GB. (a) Shear stress as a function of simulation time. (b) Snapshots of the deformation stage corresponding to the four dominant regimes in (a). Atoms with perfect fcc structures are blue, the red atoms organize the GB plane and the dislocation core, and the continuous light blue atoms represent the stacking fault. (c) Snapshots of the extracted dislocations during the shear process.

Overall, the propagation of dissociated partial dislocations from the GB plane and GB migration coupling with the shear deformation, are the deformation mechanisms of the Σ11(2 2 5)/(4 4 1) GB under shear (see movie 'S-54.74'). To the best of the authors' knowledge, the dual accommodation mechanisms of the same GB at different stress levels has not be reported very much in previous works.

3.4 The shear response of Σ11(5 5 7)/(7 7 $\bar{1}$) Φ=70.53° GB

As mentioned above, two equilibrium structures with similar GB energy were attained for Σ11(5 5 7)/(7 7 $\bar{1}$) GB. They were indexed as Φ=70.53°-A GB and Φ=70.53°-B GB (see in Fig.2). Fig.5 shows the shear stress-time curve and the corresponding stages of deformation for the Φ=70.53°-A GB. As with the asymmetric Σ11(2 2 5)/(4 4 1) GB, the shear response of bicrystal model can be divided into four dominant regimes where the onset of yielding (σ_y=0.36 GPa) is also associated with emission of dissociated dislocations from the grain boundary plane and an increased stacking fault behind. The stress curve remained almost flat during the stacking fault extension. A key result is that, after the slipping dislocations were blocked and the critical shear stress (σ_m=1.31 GPa) was reached, the GB plane did not migrate. Instead, the strain-softening resulted from the second group of dislocations that nucleated from the grain boundary (see in Fig.5-b at t=1.76 ns). Fig.5(c) shows snapshots of the extracted dislocations during the shear process. According to the analysis result, the original periodic GB structure was organized by an array of repeated GB dislocations with Burgers vector **b**=(1/3)[0 0 $\bar{1}$] and **b**=(1/3)[1 1 $\bar{1}$] along with the dissociated Shockley partial dislocations **b**=(1/6)[1 1 $\bar{2}$], as shown in Fig.5(c). During the stages of elastic, plastic, and strain-hardening, the GB kept its initial configuration until the onset of strain-softening, when another group of Shockley partial dislocations nucleated from the GB plane. The nucleation process can be described by the dislocation decomposition as:

$$(1/3)[1\ 1\ \bar{1}] \rightarrow (1/6)[1\ 1\ 0] + (1/6)[1\ 1\ \bar{2}]$$

After examining the atomic configuration we found that the nucleation of the second group of dislocations were closely correlated to the deformation of the E structural unit where one structural period of GB was extracted for analysis (see in Fig.5-d). The E unit is a kite-shape structure with six atoms involved before nucleation. These six atoms are marked with numbers 1 to 6. After the critical shear stress, atom 2 slipped out of the E unit along the (1 1 1) slip plane while the atom 4 slipped into the E unit. Eventually, this relative shift of atoms onto the opposing (1 1 1) slip plane resulted in a partial dislocation nucleation, whereas the propagation of the second group of dislocations created a 9R phase in the upper grain region (i.e. the repeat intrinsic stacking fault on every third plane). The GB structure containing the 9R phase agreed with the experimental HRTEM images of low stacking fault energy materials[45, 46].

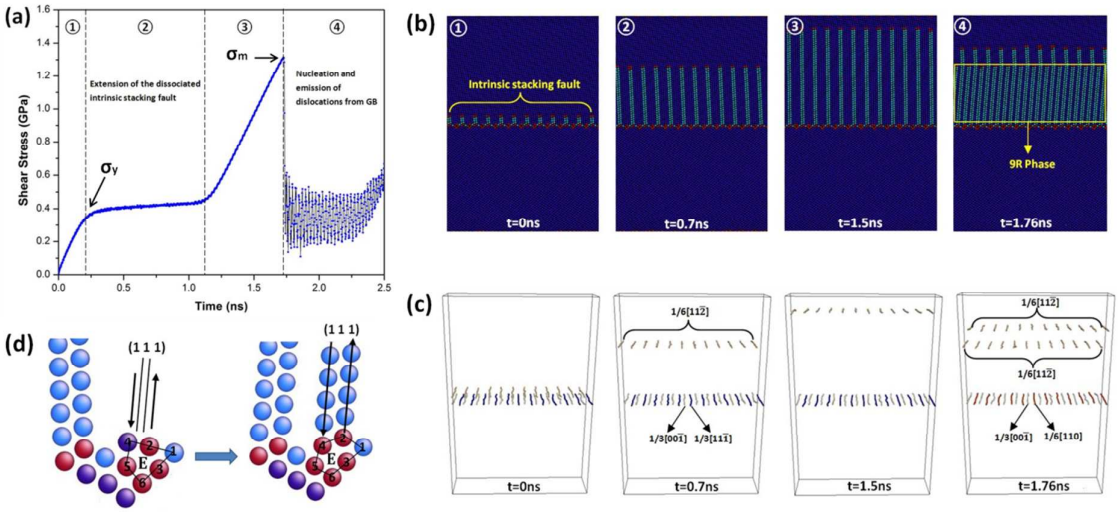

Figure-5. Shear response of Σ11(5 5 7)/(7 7 $\bar{1}$) Φ=70.53°-A GB. (a) Shear stress as a function of simulation time. (b) Snapshots of the deformation stage corresponding to the four dominant regimes in (a). Atoms of different colors represent the same as described in Fig.4. (c) Snapshots of the extracted dislocations during the shear process. (d) Enlarged view of one periodic structural unit to illustrate the deformation of E unit after dislocation nucleation.

Figure.6 shows the shear stress-time curve and the corresponding stages of deformation for the Φ=70.53°-B GB. The stress curve shows a similar trend to Φ=70.53°-A GB with the same deformation mechanisms occurring in the elastic, plastic, and strain-hardening stages (see in Fig.6-b). When the critical shear stress (σ_m=1.68 GPa) was reached, the GB plane did not migrate, and the onset of the strain-softening stage resulted from the nucleation of a second group of dislocations from the GB plane. However, unlike where Φ=70.53°-A GB, a group of extrinsic stacking faults were created after the dislocation nucleation event, where once again, one structural period of GB was extracted to present the nucleation process more clearly (see in Fig.6-d). First, the E unit was shaped like a kite at the elastic and plastic stages, and after the first group of dislocation had been stopped from slipping, the increased shear stress in the GB area rearranged the local atoms. Specifically, the free volume of the E unit was gradually shrunk by the translation of atom 4 while another E unit was under construction. The newly formed E unit is shown as E′ with the six atoms involved numbered with 1′ to 6′. Notice that the E unit and E′ unit shared two common atoms, i.e. atoms 5 & 6 in the E unit and atoms 4′ & 5′ in the E′ unit. According to the dislocation reaction analysis (see in Fig.6-c), this rearrangement of local atoms can be regarded as a combination of GB dislocations that described by:

$$(1/3)[0\ 0\ \bar{1}] + (1/3)[1\ 1\ \bar{1}] \rightarrow (1/3)[1\ 1\ \bar{2}]$$

Once the critical shear stress was reached, the relative shift of atoms 2′ & 4′ on the opposing (1 1 1) slip plane resulted in the second

partial dislocation nucleation, but note that the slip direction caused by atom 2′ in the second dislocation was opposite to that caused by the first (dissociated) dislocation. This action turned back the atoms on the overlapped plane (in the middle) to the perfect fcc position and generated an extrinsic stacking fault. This nucleation process can be described as dislocation decomposition such that:

$$(1/3)[1\ 1\ \bar{2}] \rightarrow (1/6)[1\ 1\ \bar{2}] + (1/6)[1\ 1\ \bar{2}]$$

In summary, the deformation mechanism of the Σ11(5 5 7)/(7 7 $\bar{1}$) GB under shear was the emission of the dissociated partial dislocations and the nucleation and propagation of the partial dislocations from the GB plane through to the deformation of the E structural unit. For different equilibrium boundary structures, the nucleation of the second group of partial dislocations created a 9R phase or extrinsic stacking fault in the bicrystal model with Φ=70.53°-A GB and Φ=70.53°-B GB respectively (see movie 'S-70.53-A' and 'S-70.53-B'). This partial dislocation is prone to becoming nucleated from a collapsed E structural unit and is consistent with the previous finding[21, 47]. The E unit as a dislocation source can be attributed to the intrinsic large free volume involved in it, which provides space for the arrangement of atoms to accommodate local stress concentration.

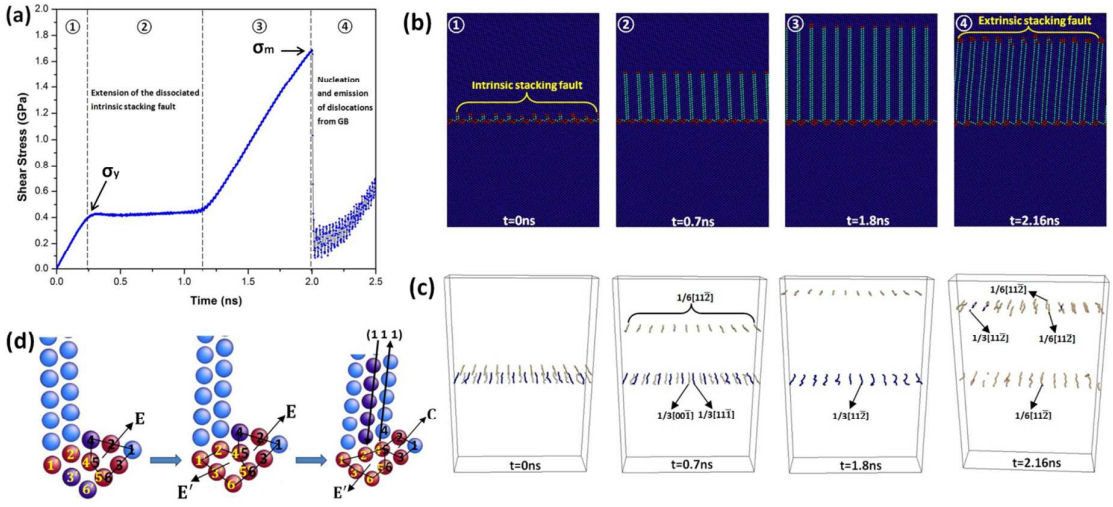

Figure-6. Shear response of Σ11(5 5 7)/(7 7 $\bar{1}$) Φ=70.53°-B GB. (a) Shear stress as a function of simulation time. (b) Snapshots of the deformation stage corresponding to the four dominant regimes in (a). Atoms of different colours represent the same as described in Fig.4. (c) Snapshots of the extracted dislocations during the shear process. (d) Enlarged view of one periodic structural unit to illustrate the deformation of E unit after dislocation nucleation.

3.5 The shear response of ∑11(3 3 2) Φ=90° GB

Fig.7 shows how the shear stress for bicrystal model evolved with the Σ11(3 3 2) symmetric GB as a function of simulation time. Snapshots of the atomic configurations of bicrystal were captured at a certain number of time steps during the straining simulations. As shear strain was applied, the bicrystal model deformed elastically (stage-1), but when the simulation cell reached a maximum level of stress (σ_m =2.08 GPa), the curve dropped abruptly from σ_m to σ_d (0.55 GPa). This relaxation in stress was associated with the grain boundary sliding. This was followed by increased shear strains with a less smooth stress profile (stage-2). When the shear stress reached another threshold value (1.81 GPa), the curve dropped again to σ_d. This behavior agreed with the so-called "stick-slip" process of GB sliding[48, 49]. While the "stick" stages corresponded to the elastic straining processes, the "slip" events should be related to some kind of structural transformation processes occurring within the bicrystal model. Fig.7(b) shows that at t=0.92 ns and t=1.6 ns indicate the GB configuration after the first and second sliding events respectively, and indicate that local atomic shuffling activities were accompanied by GB sliding during the straining process. Notice that some dislocations were nucleated in the GB area after GB sliding, but there was no dislocation slipping or GB migration (see movie 'S-90'). However, after examining the atomic configuration, the third decline in the stress curve was associated with the partial and full dislocations from the GB plane. As Fig.7(b) shows, at t=1.93 ns, two partial dislocations with Burgers vector **b**=(1/6) [$\bar{1}$ 1 $\bar{2}$] propagated from the boundary plane with an increasing stacking fault behind while a full dislocation with a leading partial **b**=(1/6) [$\bar{2}$ $\bar{1}$ 1] and a trailing partial **b**=(1/6) [$\bar{1}$ 1 2] was slipping in the lower grain area. The interaction between full and partial dislocation resulted in the shear stress fluctuating in stage-4 (see movie 'S-90').

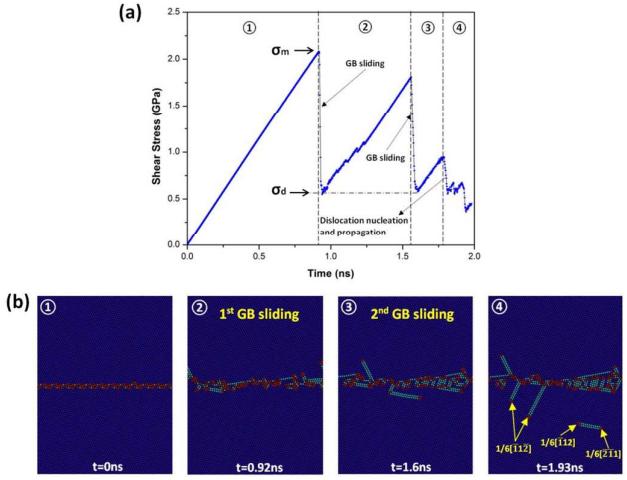

Figure-7. Shear response of Σ11(3 3 2) Φ=90° GB. (a) Shear stress as a function of simulation time. (b) Snapshots of the deformation stage corresponding to the four dominant regimes in (a). Atoms of different colours represent the same as described in Fig.4.

3.6 Evolution of the dissociated stacking fault

The length of the stacking faults at different deformation stages for the asymmetric GBs were plotted in Fig.8 as a function of simulation time. The length of the stacking fault was defined in the boundary normal direction based on the atomic coordinates of the Shockley partial dislocations in the upper grain. For the Cu bicrystal with Σ11 asymmetric GBs in this study, only a low shear stress could drive the dissociated dislocations to propagate and extend the stacking fault,

which caused the simulated models to yield and the rapid growth of the stacking fault length in Fig.8. In addition, we can see from the simulation results that these dissociated Shockley partial dislocations are pure edges, and therefore, have Burgers vectors with large y-components and small x-components. Consequently, the region swept by this array in grain-A has undergone a tilt rotation and suffered a misfit strain. These distortions significantly alter the local stress distributions, causing the stress distribution to become very nonuniform. Once this has occurred, the stress-time curve in stage-2 of Fig.4, Fig.5, and Fig.6 bears essentially no physical significance in depicting the stresses within the models. Therefore, the dislocation movement did not reduce the stress value, instead, the stress curve plateaued in the plastic stage. This indicated that the dissociated GB structure can increase ductility while retaining the high strength of the simulated cells under shear.

Moreover, The strain-hardening for asymmetric GBs that occurs once the dissociated dislocations have stopped. This action corresponds to the flat stage that occurs after a rapid growth in the length of the dissociated stacking fault, as shown in Fig.8, after which the stacking fault increased in length again for the Φ=54.74° GB because the GB migrated downwards to the lower grain. However, this did not occur for the Φ=70.53° GBs; the enlarged area in Fig.8(b) and (c) shows that the length of the first group of stacking faults decreased as the blocked dislocations began to move back, while the length of the second group of stacking faults began to increase after the dislocations nucleated from the boundary plane. This decrease in the length of the dissociated stacking faults can be attributed to the elastic interaction between the two defects. Once the length of the nucleated (2nd group) stacking faults arrived at the same level as the length of the dissociated(1st group) stacking faults, they will increase together as the shear strain increased. As was illustrated above, the nucleation of dislocations from different local GB structures resulted in the '9R phase' and 'extrinsic stacking faults' for the Φ=70.53°-A GB and Φ=70.53°-B GB respectively.

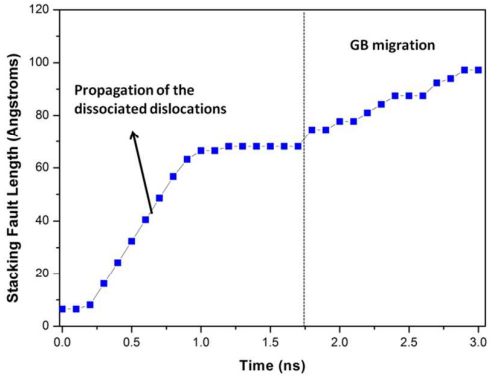

(a) Φ=54.74°

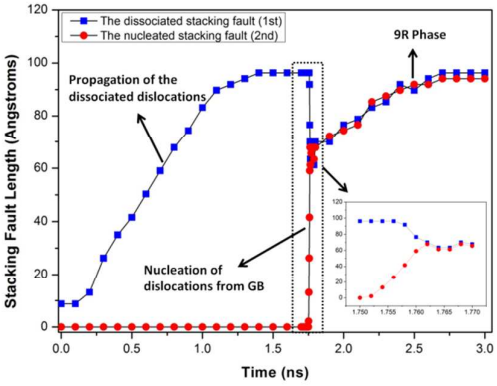

(b) Φ=70.53°-A

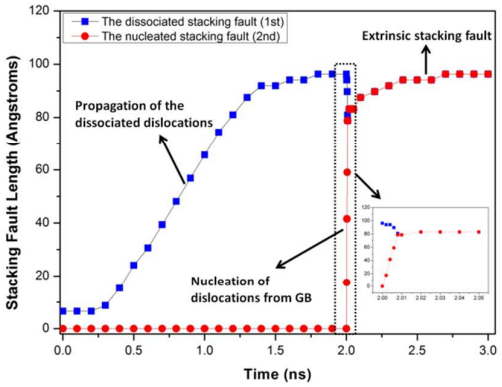

(c) Φ=70.53°-B

Figure-8. The length of stacking fault as a function of simulation time for different Σ11 asymmetric GBs. The blue squares represent the dissociated stacking fault within the equilibrium GB structures, and the red points indicate the nucleated stacking fault from the GB plane

4. Conclusion

Molecular Dynamics simulation was carried out to understand the mechanical response and deformation mechanisms of Σ11 tilt GBs in bicrystal Cu. Both symmetric and asymmetric GBs were tested under simple shear, and deformation modes were found to operate by GB migration coupled to shear deformation, with GB sliding caused by local atomic shuffling, or nucleation of dislocations and stacking faults from the GB. The results of this study can be concluded as follow.

(1) The non-planar GB structure, i.e. a GB plane with a dissociated stacking fault, was observed in the Σ11 asymmetric GBs in Cu. The dissociated structure observed in this study was mainly due to the comparative low stacking fault energy of Cu (44.4 mJ/m^2[50]). This indicated that the stacking fault energy has a significant effect on the grain boundary structure.

(2) The stress driven motion of symmetric tilt GBs was regarded as occurring by the glide of identical dislocations along parallel slip planes. This mechanism was illustrated in our simulation of the Σ11(1 1 3) symmetric GB. The coupling motion of Σ11(1 1 3) GB caused by the shear deformation can be regarded as a combination of GB dislocation (1/22)<7 4 1> and the sliding of GB dislocation (1/22)<3 3 2> along the GB plane.

(3) For the asymmetric Σ11 (Φ=54.74°) GB, shear deformation was accommodated by dislocation emissions from the GB plane, whereas GB can migrate itself at different stress level. In addition, the dislocation nucleation mechanism can be different for the asymmetric Σ11 (Φ=70.53°) GB due to its different equilibrium structures.

(4) The dissociated stacking fault from the GB plane can significantly affect the mechanical response of nanocrystalline material. It can increase ductility while retaining the high strength of the simulated cells under shear. This kind of structure can help to improve and optimize the mechanical properties by engineering the microstructure on the nanoscale in high-quality nanocrystalline metals.

Acknowledgements

This work was supported by an Australian Research Council Discovery Projects (DP130103973). Simulations were performed using the HPC cluster of University of Wollongong and the computing facilities provided by NCI National Facility of Australia. Dr. Alexander Stukowski from Darmstadt University of Technology is greatly appreciated for sharing the Crystal Analysis Tool. L.Z., L.P

and X.Z would like to acknowledge the financial support from China Scholarship Council (CSC).

References

1. Dao, M., Lu, L., Asaro, R.J., De Hosson, J.T.M. & Ma, E. *Acta Mater.* **55**, 4041-4065 (2007).
2. W olf, D., Yamakov, V., Phillpot, S.R., Mukherjee, A. & Gleiter, H. *Acta Mater.* **53**, 1-40 (2005).
3. Derlet, P.M. et al. *MRS Bull.* **34**, 184-189 (2009).
4. Farkas, D. *Curr. Opin. Solid State Mater. Sci.* **17**, 284-297 (2013).
5. Li, J. *Model. Simul. Mater. Sci. Eng.* **11**, 173-177 (2003).
6. Stukowski, A. *Model. Simul. Mater. Sci. Eng.* **18**, 015017 (2010).
7. Stukowski, A. & Albe, K. *Model. Simul. Mater. Sci. Eng.* **18**, 085001 (2010).
8. Stukowski, A. *Model. Simul. Mater. Sci. Eng.* **20**, 045021 (2012).
9. Stukowski, A., Bulatov, V.V. & Arsenlis, A. *Model. Simul. Mater. Sci. Eng.* **20**, 085007 (2012)..
10. Van Swygenhoven, H., Derlet, P.M. & Hasnaoui, A. *Adv. Eng. Mater.* **5**, 345-350 (2003).
11. Sansoz, F. & Molinari, J.F. *Scr. Mater.* **50**, 1283-1288 (2004).
12. Sansoz, F. & Molinari, J.F. *Acta Mater.* **53**, 1931-1944 (2005).
13. Cahn, J.W., Mishin, Y. & Suzuki, A. *Acta Mater.* **54**, 4953-4975 (2006).
14. Wan, L. & Wang, S. *Phys. Rev. B* **82**, 214112 (2010).
15. de Koning, M. et al. *J. Nucl. Mater.* **323**, 281-289 (2003).
16. de Koning, M., Miller, R., Bulatov, V.V. & Abraham, F.F. *Philos. Mag.* **82**, 2511-2527 (2002).
17. Jin, Z.H. et al. *Acta Mater.* **56**, 1126-1135 (2008).
18. Jin, Z.H. et al. *Scr. Mater.* **54**, 1163-1168 (2006).
19. Spearot, D.E., Jacob, K.I. & McDowell, D.L. *Acta Mater.* **53**, 3579-3589 (2005).
20. Spearot, D.E., Jacob, K.I. & McDowell, D.L. *Int. J. Plast.* **23**, 143-160 (2007).
21. Spearot, D.E., Tschopp, M.A., Jacob, K.I. & McDowell, D.L. *Acta Mater.* **55**, 705-714 (2007).
22. Bachurin, D.V., Weygand, D. & Gumbsch, P. *Acta Mater.* **58**, 5232-5241 (2010).
23. Tschopp, M.A. & McDowell, D.L. *Int. J. Plast.* **24**, 191-217 (2008).
24. Zhang, L., Lu, C. & Tieu, K. *Sci. Rep.* **4** (2014).
25. Trautt, Z.T., Adland, A., Karma, A. & Mishin, Y. *Acta Mater.* **60**, 6528-6546 (2012).
26. Zhang, H., Duy, D. & Srolovitz, D.J. *Philos. Mag.* **88**, 243-256 (2008).
27. Fensin, S.J., Asta, M. & Hoagland, R.G. *Philos. Mag.* **92**, 4320-4333 (2012).
28. Plimpton, S. *J. Comput. Phys.* **117**, 1-19 (1995).
29. Mishin, Y., Mehl, M.J., Papaconstantopoulos, D.A., Voter, A.F. & Kress, J.D. *Phys. Rev. B* **63**, 2241061-22410616 (2001).
30. Rittner. *Phys. Rev. B* **54**, 6999-7015 (1996).
31. Tschopp, M.A. & McDowell, D.L. *Philos. Mag.* **87**, 3147-3173 (2007).
32. Olmsted, D.L., Foiles, S.M. & Holm, E.A. *Acta Mater.* **57**, 3694-3703 (2009).
33. Zhang, L., Lu, C., Michal, G., Tieu, K. & Cheng, K. *Mater. Res. Express* **1**, 015019 (2014).
34. Schiøtz, J., Di Tolla, F.D. & Jacobsen, K.W. *Nature* **391**, 561-563 (1998).
35. Tschopp, M.A. & McDowell, D.L. *Philos. Mag.* **87**, 3871-3892 (2007).
36. Cui, C.B. & Beom, H.G. *J. Mater. Sci.* **49**, 8355-8364 (2014).
37. Rittner. *Phys. Rev. B* **54**, 6999-7015 (1996).
38. Rae, C.M.F. & Smith, D.A. *Philos. Mag.* **41**, 477-492 (1980).
39. Fukutomi, H. & Kamijo, T. *Scr. Metall* **19**, 195-197 (1985).
40. Yamakov, V., Wolf, D., Phillpot, S.R., Mukherjee, A.K. & Gleiter, H. *Nature mater.* **1**, 45-48 (2002).
41. Van Swygenhoven, H. & Weertman, J.R. *Mater. Today* **9**, 24-31 (2006).
42. Read, W.T. & Shockley, W. *Phys. Rev.* **78**, 275-289 (1950).
43. Molodov, D.A., Gorkaya, T. & Gottstein, G. *J. Mater. Sci.* **46**, 4318-4326 (2011).
44. Syed, B., Catoor, D., Mishra, R. & Kumar, K.S. *Philos. Mag.* **92**, 1499-1522 (2012).
45. Ernst, F. et al. Theoretical predication and direct observation of the 9R structure in Ag. *Phys. Rev. Lett.* **69**, 620-623 (1992).
46. Wolf, U., Ernst, F., Muschik, T., Finnis, M.W. & Fischmeister, H.F. *Philos. Mag.* **66**, 991-1016 (1992).
47. Tucker, G.J., Tschopp, M.A. & McDowell, D.L. *Acta Mater.* **58**, 6464-6473 (2010).
48. Mishin, Y., Suzuki, A., Uberuaga, B.P. & Voter, A.F. *Phys. Rev. B* **75**, 224101 (2007).
49. Hu, Q., Li, L. & Ghoniem, N.M. *Acta Mater.* **57**, 4866-4873 (2009).
50. Mishin, Y., Farkas, D., Mehl, M.J. & Papaconstantopoulos, D.A. *Phys. Rev. B* **59**, 3393-3407 (1999).